



UNIVERSITY OF LEEDS

This is a repository copy of *Secular variation in seawater redox state during the Marinoan Snowball Earth event and implications for eukaryotic evolution*.

White Rose Research Online URL for this paper:

<https://eprints.whiterose.ac.uk/188204/>

Version: Supplemental Material

Article:

Shen, W, Zhu, X, Yan, B et al. (3 more authors) (2022) Secular variation in seawater redox state during the Marinoan Snowball Earth event and implications for eukaryotic evolution. *Geology*, 50 (11). pp. 1239-1244. ISSN 0091-7613

<https://doi.org/10.1130/G50147.1>

© 2022 Geological Society of America. This is an author produced version of an article published in *Geology*. Uploaded in accordance with the publisher's self-archiving policy.

Reuse

Items deposited in White Rose Research Online are protected by copyright, with all rights reserved unless indicated otherwise. They may be downloaded and/or printed for private study, or other acts as permitted by national copyright laws. The publisher or other rights holders may allow further reproduction and re-use of the full text version. This is indicated by the licence information on the White Rose Research Online record for the item.

Takedown

If you consider content in White Rose Research Online to be in breach of UK law, please notify us by emailing eprints@whiterose.ac.uk including the URL of the record and the reason for the withdrawal request.



eprints@whiterose.ac.uk
<https://eprints.whiterose.ac.uk/>

Supplemental Materials

Secular variation in seawater redox state during the Marinoan Snowball

Earth event and implications for eukaryotic evolution

Weibing Shen, Xiangkun Zhu, Bin Yan, Jin Li, Pengju Liu, Simon W. Poulton

The WORD file includes:

- **Text S1: Geological Setting and Study Section Description**

- **Text S2: Glaciation System**

- **Text S3: Materials and Methods**

- **Text S4: Background and Interpretation of Geochemical Data**

- **Text S5: Alternative Hypotheses for Seawater Redox Variability**

- **Figure S1:** Global reconstruction of the location of the Yangtze block and stratigraphic division of the Neoproterozoic transect in the Yangtze block.

- **Figure S2:** Morphology of pyrite for Nantuo Formation in South China.

- **Figure S3:** Photographs showing lithofacies of the Nantuo Formation from the ZK01 core section.

- **Figure S4:** Model showing pyrite formation in the water column and sediments under oxic, ferruginous, and euxinic conditions.

- **References Cited**

19 **Text S1: Geological Setting and Study Section Description**

20 **Geological Setting**

21 South China consists of two tectonic units: The Cathaysia block in the present southeast, and
22 the Yangtze block in the present northwest (Fig. 1a). The Yangtze block was an independent
23 continental block during the late Neoproterozoic, with direct connection to the open ocean to the
24 southwest (Wang and Li, 2003; Fig. S1a).

25 Our samples from the Nantuo Formation were collected from a drill core (ZK01) from Taojiang
26 city in northwestern Hunan Province, Yangtze block of South China (Fig. 1a). Neoproterozoic strata
27 (Tonian strata, Cryogenian strata and Ediacaran strata) are well preserved on the Yangtze block, with
28 some of the best age constraints in the world (Jiang et al., 2011; Fig. S1b). The Cryogenian strata
29 include two glacial units separated by an interglacial interval (Zhang et al., 2011). The Chang'an
30 Formation/Fulu Formation/Gucheng Formation/Tiesi'ao Formation, correspond to the Sturtian
31 glaciation (ca.720-659 Ma; Wang and Li, 2003; Lan et al., 2015; Wang et al., 2019), and are mainly
32 composed of diamictites. The interglacial strata, represented by the Datangpo Formation/Xiangmeng
33 Formation, deposited from ca. 659 Ma to ca. 649 Ma (Zhou et al., 2018; Bao et al., 2018; Wang et
34 al., 2019), and mainly comprise shale and siltstone with local manganese deposits (Zhang et al.,
35 2015; Peng et al., 2019). The Nantuo Formation corresponds to the Marinoan glaciation, and mainly
36 comprises glacial diamictite deposited between ca. 649 Ma to ca. 635 Ma (Condon et al., 2005; Zhang
37 et al., 2008; Zhang et al., 2011; Schmitz 2012; Zhou et al., 2018; Bao et al., 2018; Wang et al., 2019).
38 The Nantuo Formation, the target strata, has a wide distribution across the Yangtze block (Fig. 1b).
39 The thickness of this unit varies significantly, from 60-100 m in shallow water settings such as the
40 Hubei Yangtze Gorges area, through 200-300 m in slope settings such as the Guizhou Daotuo area,

41 to a few thousand meters in basin settings such as the Hunan Tongdao area (Fig. S1b; Wang and Li,
42 2003; Zhang et al., 2011).

43 As a whole, the Cryogenian Nantuo Formation has a conformable contact with the cap
44 carbonate rocks of the overlying Ediacaran Doushantuo Formation across a basin-wide transect (Fig.
45 S1b; Jiang et al., 2011; Lang et al., 2018a). Although the lithofacies of the two formations are
46 obviously different, a conformable contact is observed (Lang et al., 2018a; Yan et al., 2020; Shen et
47 al., 2021). On the one hand, as shown by a gradual upward increase in the calcareous content of the
48 rocks in the top part of the Nantuo Formation, the lower glacial deposits progressively transform into
49 a cap carbonate (Lang et al., 2018a; Yan et al., 2020; Shen et al., 2021). On the other hand, clastic
50 gravels often appear at the bottom of the cap carbonate, representing a continuous transition between
51 glacial and post-glacial deposits (Lang et al., 2018a; Yan et al., 2020; Shen et al., 2021).

52 The contact relationship between the Nantuo Formation and underlying non-glacial strata in
53 the research area is complicated (Figs. 1b and S1b; Zhang et al., 2008; Peng et al., 2019; Yan et al.,
54 2020; Shen et al., 2021). In shallow water settings, the Nantuo Formation has an unconformable
55 contact with purple-red sandstone of the Liantuo Formation (Zhang et al., 2008; Peng et al., 2019;
56 Yan et al., 2020; Shen et al., 2021). An unconformity between the Nantuo Formation and the Liantuo
57 Formation is shown by deformation structures (Zhang et al., 2008; Peng et al., 2019; Shen et al.,
58 2021). In slope-basin settings, the Nantuo Formation has a conformable contact with black shale of
59 the Datangpo Formation/Xiangmeng Formation (Zhang et al., 2008; Peng et al., 2019; Yan et al.,
60 2020; Shen et al., 2021). Although there are large changes in gravel content and size between the
61 Nantuo Formation diamictite and the underlying interglacial shale of the Datangpo
62 Formation/Xiangmeng Formation, no unconformity is observed. Instead, a gradual transition between

63 the two formations is evident in terms of colour, organic content and general lithology (Zhang et al.,
64 2008; Peng et al., 2019; Yan et al., 2020; Shen et al., 2021).

65 **Study Section Description**

66 The ZK01 core documents a slope-basin setting (Fig. 1a), and the Nantuo Formation from the
67 core has a conformable contact with the underlying interglacial Datangpo Formation mudstone and
68 the overlying Ediacaran Doushantuo Formation carbonate (Figs. S1b and 2). Thus, the Nantuo
69 Formation recovered from the core section was deposited during the Marinoan glaciation (Fig. 2).

70 The Nantuo Formation in ZK01 is about 295 m thick, and mainly comprises diamictite
71 lithofacies, with local fine-grained lithofacies (Fig. 2). The diamictite lithofacies in the Nantuo
72 Formation contains abundant pyrite (Fig. 2 and S2), and is mainly composed of dark gray gravel-
73 bearing carbonaceous sandstone, light gray gravelly siltstone, and dark gray-light gray siltstone (Figs.
74 2 and S3). This lithofacies is entirely matrix-supported and the gravels are poorly sorted, disordered,
75 and angular-shaped (subangular-circular and subangular dominate) (Figs. 2 and S3). The composition
76 of the gravels is diverse, although it is dominated by sandstone gravels and basic rock gravels. The
77 gravel content of the diamictite is generally greater than 5%, and locally greater than 30%. The gravel
78 sizes range from 2 mm to nearly 5 cm, with mm-scale size dominating. We emphasize here that the
79 gravel size and content show regular changes throughout the Nantuo Formation, marking two
80 lithological cycles (Fig. 2).

81 At the base, the Nantuo Formation from the core section conformably overlies the black shale
82 of the interglacial Datangpo Formation (Figs. 2 and S3). The first lithological cycle (0-125 m), begins
83 with a gravel sandy-mudstone interval, and mainly consists of dark-gray gravel-bearing carbonaceous
84 siltstone in the lower part, dark-grey gravelly sandstone in the middle part, and grey sandstone and

85 gravel-bearing siltstone in the upper part (Fig. 2). The gravel contents vary from < 10% at the bottom,
86 through 30% in the middle, to < 10% at the top. Correspondingly, gravel sizes change from 0.2-1.5
87 cm, to 2.0-3.0 cm, and then back to 0.5-1 cm. The first cycle, as an entire shallowing-deepening
88 sequence, ends with a ca. 4 m thickness of carbonate rock interval (Figs. 2 and S3). The second cycle
89 (ca 125-295 m) mainly consists of light-grey gravel-bearing siltstone in the lower part, grey gravelly
90 sandstone in the middle part, and light-grey calcareous gravel-bearing siltstone in the upper part.
91 Similar to the first cycle, both the gravel content and size in this cycle first increase and then decrease.
92 The gravel contents range from 0% to 25%, occasionally reaching 35%. Gravel sizes concentrate
93 around 0.2-3 cm (generally 0.5-1 cm) (Fig. 2). The regular changes in gravel content and size indicate
94 another entire shallowing-deepening sequence. At the top of the Nantuo Formation, post-glacial cap
95 carbonate rocks of the Ediacaran Doushantuo Formation conformably overlie the diamictite (Figs. 2
96 and S3).

97 **Text S2: Glaciation System**

98 **Glacial Sedimentology**

99 Sedimentological characteristics of the Cryogenian successions are essential for interpreting
100 the paleoenvironment in which these deposits formed. Based on distance from the ice grounding line,
101 glacial facies can mainly be classified into ice-contact facies association, proximal glacial-marine
102 facies association, and distal glacial-marine facies association (Boulton and Deynoux, 1981; Naish et
103 al., 2009; Lang et al., 2018a). As is common in glacial sediments, proximal glacial-marine facies and
104 distal glacial-marine facies are observed in the Cryogenian successions of South China.

105 The proximal glacial-marine facies association is mainly reflected by an assemblage of deposits
106 formed near the ice grounding line (Brodzikowski and Van Loon, 1987). The sediments mainly

107 consist of meter-scale massive diamictite lithofacies and gravel-containing sandstones, which are
108 usually deposited from gravity flow debris and rainout of ice-rafted debris transported by glaciers.
109 The proximal glacial-marine facies association can be observed in the Nantuo Formation at multiple
110 sections in South China, and mainly consists of thick massive diamictites (Fig. 1b; Shen et al., 2021).
111 For example, evident massive diamictite lithofacies are developed in the lower part of the Nantuo
112 Formation in the ZK01 core section, with thicknesses of more than 10 m (Fig. 2). When the flow
113 pattern of subglacial meltwater drainage changes in the proximal glacialmarine environment, the
114 resultant lithofacies will transform. This is shown by the transformation of thick massive diamictite
115 lithofacies into other lithofacies, such as weakly sorted massive diamictite, gravel-bearing sandstones,
116 and siltstones. There are many lithofacies transformations in the Nantuo Formation of South China.
117 For example, in the upper part of the Nantuo Formation in the ZK01 core section, there are multiple
118 massive diamictite-gravel sandstone cycles, which can be classified as a proximal glacial-marine
119 facies association.

120 The distal glacial-marine facies association represents a set of sedimentary rocks formed in the
121 environment far from the ice grounding line (Brodzikowski and Van Loon, 1987). This facies
122 association can be observed in the Nantuo Formation at multiple sections in South China and mainly
123 includes meter-scale massive diamictite lithofacies, gravel-containing fine-grained sandstones, and
124 drop-stone lithofacies. For example, drop-stone lithofacies were observed in the Nantuo Formation
125 at the Shennongjia section, South China (Fig. 1d). Because the distal glacial-marine environment is
126 far from the ice grounding line, low density flow debris and gravity flow debris were deposited, with
127 local transient medium or high density flow debris. Once the debris was carried to the area near the
128 grounding line, it was deposited due to jet flows. Subsequently, the jet-flow deposits can be reworked

129 by flows in the shallow-water environment, winnowing the fine fraction and leaving gravel-bearing
130 sandstones. Types of flow debris can be reflected by heterogeneous lithofacies: The coarse-grained
131 sandstones with gravel always show high density flow debris, while the overlying sandstones and
132 silts represent low density flow debris in a deeper water environment. The gravel-bearing coarse-
133 grained sandstones in the Nantuo Formation in the ZK01 core section were likely deposited from
134 high-density debris flows, which formed in a distal glacialmarine environment (Figs. 2 and S3). In
135 addition, shales, siltstones and carbonates may be directly deposited from seawater with little glacial
136 influence (Tucker et al., 1990; Łabaj and Pratt, 2016; Lang et al., 2018a), possibly in the distal
137 glaciomarine environment or localised open water environment, as proposed by other studies (Lang
138 et al., 2018a; Bai et al., 2020; Shen et al., 2021).

139 Based on sedimentary characteristics of the Nantuo Formation across a basin-wide transect,
140 there is not only massive diamictite in the proximal glacial environment, but also gravel-containing
141 fine-grained sediments in the distal glacial environment or the normal sea environment in South China
142 (Fig. 4, Shen et al., 2021). The variations in the sedimentary facies of the Nantuo Formation in South
143 China indicate that sedimentation was active during the glaciation.

144 **Glaciation Dynamics**

145 The initial ‘Snowball Earth’ hypothesis posited a simple, stagnant glaciation, characterized by
146 extremely cold climate, and hence an entirely frozen Earth during the Cryogenian period (Kirschvink
147 1992; Hoffman et al., 1998). Although the ‘Snowball Earth’ hypothesis has become widely accepted
148 (Hoffman and Schrag 2002; Boyle et al., 2007; Rooney et al., 2015), the interpretation of the simple,
149 stagnant nature of the prolonged glaciations remains controversial. Debate has mainly focused on the
150 interpretation of sedimentological records of glaciogenic strata throughout the Cryogenian ice age,

151 with data that indicate that the glaciations were dynamic rather than stagnant, and were associated
152 with a relative strong climate and hydrological cycle.

153 The dynamic nature of the Cryogenian glaciation originally came from climate modeling. Hyde
154 (2000) proposed rapid transitions into and out of a full glaciation, associated with decreased and
155 increased temperatures, and an equatorial belt of open water that may have occurred during the
156 ‘Snowball Earth’ event. The temperature fluctuations and changes in ice sheet extent were also
157 deduced from follow-up simulations (Liu et al., 2020). These modeling results find support in
158 sedimentary evidence. The key sedimentary records were vertical lithofacies alternations (Le Heron
159 et al., 2014; Lang et al., 2018a; Hu et al., 2020; Yan et al., 2020). For example, studies from the
160 Marinoan deposits in South China provide the basis for establishing a sequence stratigraphic
161 framework that includes two complete glacial cycles across a basin-to-platform transect (Fig. 1b;
162 Shen et al., 2021). Both cycles are characterized by repetition of glacially influenced units separated
163 by non-glacial units. In addition, cyclic depositions of Marinoan units have been reported from
164 elsewhere, such as Central Siberia (Chumakov, 2009), Oman (Allen and Etienne, 2008), Norway
165 (Halverson et al., 2004), Southwest China (He et al., 2007), South Australia (Williams et al., 2008),
166 and Scotland (Arnaud and Eyles, 2006). It is proposed that facies changes of the glacial deposits could
167 be induced by excessive topography relief during the global glaciation (Hoffman et al., 2017b). In
168 this scenario, deposition of diamictite during ice sheet melting may both create and destroy small-
169 scale topography, resulting in short-distance migration of the depocenter and complexity in the
170 stratigraphic detail of the glacial deposits. In particular, oversteepening of diamictite could generate
171 reworked sediments, such as crudely stratified diamictite, pebbly sandstone and stratified sandstone
172 (Hoffman et al., 2017b). This scenario seems to be a good explanation for variable thickness and

173 vertical facies change of glacial deposits within a short distance. However, it cannot explain the
174 stratigraphic variation of facies in the Nantuo Formation, which can be correlated across the Yangtze
175 block and has a basin-wide scale (Lang et al., 2018a; Shen et al., 2021). Further, the thick non-glacial
176 sequences (tens of meters) of siltstone/mudstones and carbonate beds in the Nantuo Formation cannot
177 simply be interpreted as deposits during ice sheet melting (Fig. 1b; Allen and Etienne, 2008; Lang et
178 al., 2018a; Gu et al., 2019). Instead, the massive diamictite and pebbly sandstone were precipitated
179 during the melting of ice sheet (Allen et al., 2004), while the clasts-free finegrained
180 mudstone/siltstone and sandstone represented normal marine deposition with siliciclastic sediments
181 transported by water currents (Talling et al., 2012). Thus, the repetition of glacially influenced units
182 separated by non-glacial units in the Nantuo Formation records ice-sheet advancing-retreating cycles
183 (Lang et al., 2018a; Bai et al., 2020; Shen et al., 2021).

184 Sedimentary records are a comprehensive reflection of paleoclimate changes and sea level
185 fluctuations (Hoffman and Schrag 2002). When the paleoclimate was cold, ice sheets would form,
186 sea level would drop, and hence the ice grounding line would advance seaward. Consequently, ice
187 advance successions dominated by a proximal glacial lithofacies association would be deposited, and
188 the gravel content and size of the rocks are increased (Lang et al., 2018a; Shen et al, 2021). By contrast,
189 when the paleoclimate warmed, the ice grounding line would retreat and sea level would rise. As a
190 result, ice retreat successions dominated by distal glacial lithofacies association would develop, and
191 the gravel content and size of the rocks decreases (Lang et al., 2018a; Shen et al, 2021). Thus, the
192 above-mentioned sedimentological records, interpreted to reflect gradual alternation from ice
193 advance to ice retreat, indicates dynamic co-evolution of the sedimentary environment, paleoclimate,
194 and sea level during the Marinoan glaciation (Lang et al., 2018a; Yan et al., 2020; Bai et al., 2020;

195 Shen et al., 2021).

196 The Marinoan deposits of the slope-basin ZK01 setting in South China also have two complete
197 glacial cycles (Fig. 2). The lower ice-advance succession of the glacial cycles consists primarily of a
198 massive diamictite lithofacies association, and is dominated by proximal glaciomarine deposits. The
199 gravel abundance and size of the deposits gradually increase upwards, suggesting a shallowing
200 sequence. The upper ice-retreat succession of the glacial cycles is composed of both a massive
201 diamictite lithofacies association and a fine-grained lithofacies association, representing a mix of
202 distal glaciomarine, proximal glaciomarine, and non-glacial marine deposits. The gravel abundance
203 and size of these varied deposits gradually decreases upwards, and is interpreted to reflect a deepening
204 sequence. These glacial cycles imply that the climate switched twice from relatively warm to
205 extremely cold and back during the Marinoan glaciation, associated with sea level fluctuations (Figs.
206 1, 2, and 4).

207 **Meltwater Supply**

208 Glacial meltwater can be divided into three categories: meltwater on the ice sheet surface
209 (atmospheric temperature), meltwater at the basal ice sheet (surface heat flow and pressure), and
210 meltwater at the base of the ice shelf (seawater temperature). The meltwater can form significant
211 drainage on the surface, internal and base of the glacier (Irvine-Fynn et al., 2011). Some of the
212 meltwater drainage on the ice sheet surface can reach the basal ice sheet through connected crevasses
213 and holes inside the glacier (Skidmore and Sharp, 1999). During the ‘Snowball Earth’ event,
214 subglacial meltwater drainage likely mainly consisted of meltwater from the basal ice sheet and the
215 basal ice shelf, with relatively little from the ice sheet surface.

216 Meltwater supply is closely related to the glacier thermal regime (Paterson, 2016), which is

217 controlled by air temperature (climate), geothermal flux, and pressure/friction (ice thickness) (Irvine-
218 Fynn et al., 2011). When the geothermal flux and pressure are large (the glacier thickness is large),
219 the glacier thermal regime would be warm, and there is a large amount of meltwater at the bottom of
220 the glacier. Usually, connected meltwater drainages would occur at the warm basal ice sheet, causing
221 the glacier to move quickly, thus depositing a large unit of glacial diamictite (Piotrowski, 1997).
222 Conversely, the glacier thermal regime is colder when the geothermal flux and pressure are small. A
223 cold glacier has less meltwater at the glacier base, and is mostly moved by internal ice deformation
224 (Tranter et al., 1997). Generally, a thick ice sheet near the ice grounding line, where there is the fastest
225 melting rate of glaciers, generates the largest amount of meltwater to form connected meltwater
226 drainage (Lewis and Perkin, 1986). Glacial sedimentology and the relative abundance of different
227 glacial facies can be used to interpret the thermal regime of ancient glaciers (Hambrey et al., 2012).
228 Our sedimentary evidence above (Figs. 1b and 4) and previous studies have shown that Cryogenian
229 glaciation with abundant diamictite may be a warm regime, leading to effective meltwater drainage
230 in the South China region (Hu et al., 2020; Shen et al., 2021).

231 It is worth emphasizing that the amount of glacial meltwater supply varies with ice sheet
232 dynamics (Hoffman et al., 2017). During the ice retreat period, the thickness of the glacier decreases
233 and the amount of meltwater supply increases (Fig. 4). Meltwater production rates during this period
234 may be an order of magnitude higher than the mean global runoff rate (Shields, 2005). A large amount
235 of meltwater during this period can result in channelized meltwater drainage, which efficiently flows
236 to the glaciomarine environment, discharging at the grounding line as focused meltstream exits
237 (Piotrowski, 1997). During the ice advance period, the thickness of the ice sheet increases, the amount
238 of meltwater supply decreases, and subglacial meltwater drainages are more widely distributed (Fig.

239 4). The distributed system is far less efficient than the channelized system, leading to longer meltwater
240 residence times (Tranter et al., 1997).

241 **Meltwater Derived-oxygen/sulfate**

242 During the ‘Snowball Earth’ event, the global glaciation would have effectively ceased surface
243 water–air/land communication, resulting in the extreme suppression of chemical cycles, including
244 atmospheric oxygen and the continental sulfate influx (Kirschvink, 1992; Hoffman et al., 1998).
245 However, injection of meltwater and the resultant drainage/stream generated beneath ice sheets can
246 deliver sufficient dissolved oxygen and sulfate into the subglacial ocean (Liang et al., 2006; Anderson,
247 2007; Lechte et al., 2019).

248 Air bubbles trapped within the snow (meteoric ice) would be compressed into glacial ice
249 (Hoffman et al., 2017). Upon melting of the glacier, either by increased air temperatures, geothermal
250 fluxes, pressure or friction, meltwater would contain O₂ dissolved from the trapped air bubbles
251 (Hoffman et al., 2017), as seen in modern Alpine glacial meltwater (Brown et al., 1994). Although
252 this O₂ influx is supposed to be substantially offset by consumption of O₂ via either microbial or
253 abiotic processes, such as seafloor weathering (Le Hir et al., 2008a), the remaining O₂ influx may be
254 substantial (Anderson, 2007). Particularly, during the ice sheet retreat period, ice sheets melt
255 significantly and channelized meltwater drainage is formed, and meltwater can convey O₂ to the
256 subglacial environment (Jenkins, 1999), thus changing chemical properties such as seawater
257 oxygenation (Le Hir et al., 2008a; Lechte et al., 2019).

258 Through a combination of friction and plucking, glaciers constantly erode the bedrock to form
259 a large quantity of sediment, which fill the subglacial depositional space (Anderson, 2007). Due to
260 the rapid rate of denudation and fine-textured nature of the sediments, glacial erosion produces a very

261 high overall mineral surface area. The substantial mineral surface area from glacial erosion
262 significantly accelerates subglacial chemical weathering, and delivers a large amount of dissolved
263 ions into glacial seawater via meltwater (Armstrong, 1971). For many glaciers, such as the Cascade
264 Glacier, the ion influx related to subglacial weathering has been measured. These studies show that
265 the total ion influx during the glaciation is generally in excess of the normal global mean (Hallet et
266 al. 1996). As a major type of ion delivered into the subglacial seawater, sulfate, mainly derived from
267 the oxidation of sulfide, accounts for about 10-25% of the total ion influx (Sharp et al. 1995; Anderson
268 et al. 2000; Anderson et al. 2003). For example, at Bench Glacier (Alaska) on metamorphic
269 sedimentary rocks, sulfate from the oxidation of sulfides accounts for 23% of the total ion influx into
270 the ocean (Anderson et al. 2000). Thus, meltwater derived sulfate likely provided a significant flux
271 to the Cryogenian subglacial ocean (Anderson, 2007; Hoffman et al., 2017).

272 Because the amount of meltwater discharge exerts an important control on subglacial oxygen
273 (Liang et al., 2006; Lechte et al., 2019) and dissolved ion influx (Collins & MacDonald, 2004), it is
274 most instructive to consider oxygen and sulfate fluxes as a function of water discharge (Anderson,
275 2007). With the glaciation dynamics and the associated dynamic meltwater supply, the delivery of
276 dissolved oxygen and sulfate from meltwater generated beneath ice sheets varies with the ice advance
277 and retreat (Fig. 4).

278 **Text S3: Materials and Methods**

279 **Sample Description and Preparation**

280 Samples for analysis of pyrite morphology, Fe-speciation, TOC and pyrite Fe-S isotopes were
281 collected throughout the Nantuo Formation in the ZK01 core section of the Yangtze block, South
282 China. Fragments of core samples were divided into two sub-samples, one for thin-section and

283 handpicking of pyrite grains, and the other for geochemical analyses.

284 Thin-sections (polished, 0.5-mm-thick) were used to investigate pyrite morphology. Pyrite,
285 which is evident as larger euhedral grains in hand specimen (Fig. S2), is abundantly distributed
286 throughout the Nantuo Formation. Under the optical and scanning electron microscope (SEM), pyrite
287 morphologies vary, and include euhedral, subhedral, aggregates, disseminated pyrite and pyrite
288 framboids (Figs. 2 and S2). A sample can contain more than one pyrite type, but euhedral and
289 subhedral pyrite represent the dominant morphologies. The euhedral and subhedral pyrite are
290 dominated by square and triangular pyrite, indicating a likely diagenetic origin. By contrast, detrital
291 pyrite, which would be expected to have rounded grain boundaries, was not observed in the Nantuo
292 Formation.

293 Prior to geochemical analyses of Fe-speciation and TOC, the matrix was sampled (finer grained
294 sediments) in the bulk-rock samples to avoid larger clasts. Then, the matrix was powdered to <74 μm
295 and preserved in a desiccator after being dried at 80°C for 3 h.

296 **Total Organic Carbon (TOC)**

297 TOC was determined at the State Key Laboratory of Petroleum Resources and Prospecting,
298 China. To remove carbonate minerals, an appropriate amount of 10% HCl was used to dissolve the
299 powdered matrix sample (about 0.5 g). The residue was washed with ultrapure water and then dried
300 in a desiccator for 10 h at 60°C, followed by combustion at 900°C to oxidize organic carbon in a pure
301 oxygen atmosphere. The resultant carbon dioxide was subsequently measured to provide the TOC
302 data, using a LECO CS-230 carbon analyzer, and the detailed analytical procedure can be found in
303 Zhao (2019).

304 **Iron Speciation**

305 Total iron (Fe_T) can be divided into three fractions: highly reactive iron (Fe_{HR} , representing the
306 Fe fraction that is potentially reactive towards sulfidation in the water column and during diagenesis;
307 Poulton and Canfield, 2011), poorly reactive iron (Fe_{PR}), and unreactive iron (Fe_U). Fe_{HR} includes: (1)
308 iron associated with carbonate minerals (Fe_{carb} ; siderite, ankerite); (2) ferric (oxyhydr)oxide minerals
309 (Fe_{ox} ; ferrihydrite, lepidocrocite, goethite, hematite); (3) magnetite (Fe_{mag}); and (4) Fe sulfide (Fe_{py} ;
310 pyrite) (Poulton and Canfield, 2005; Poulton and Canfield, 2011). Iron speciation analyses were
311 performed at the University of Leeds, UK. Total Fe was extracted using a standard multi-acid
312 digestion (HNO_3 – HCl – HF) (Alcott et al., 2020), and the sequential extraction of Fe_{carb} , Fe_{ox} and Fe_{mag}
313 was performed according to Poulton and Canfield (2005). All Fe concentrations were determined by
314 atomic absorption spectrometry (AAS). Fe_{py} was extracted and measured at China University of
315 Geosciences, Wuhan, via the chromous chloride reduction method of Canfield et al. (1986), with
316 concentrations determined gravimetrically following precipitation of H_2S as Ag_2S . Accuracy and
317 precision of all Fe phases was ensured by replicate extractions of international Fe speciation standard
318 (Alcott et al., 2020), with a relative standard deviation of < 5% for all Fe pools.

319 **Pyrite Sulfur Isotopes**

320 Prior to sulfur isotope analysis, optical and scanning electron microscopy (SEM) were used
321 to choose the pyrite crystals, and euhedral grains (> 50 μm) were selected. Thin sections with eligible
322 pyrite grains were set into a sample cell coupled to the test instrument. Determination of sulfur isotope
323 compositions was carried out by spot analysis, using a LA-MC-ICP-MS at the State Key Laboratory
324 for Mineral Deposits Research, China, comprising a New WaveTM ArF excimer laser ablation system
325 (UP-193FX, 193 nm, Fremont, America) coupled with a Neptune plus MC-ICP-MS (Thermo Fisher

326 Scientific™, Bremen, Germany). The operational conditions of the laser system and the MC-ICP-MS
327 are from Zhu et al. (2016, 2017). An in-house pyrite standard (WS-1 with a $\delta^{34}\text{S}_{\text{V-CDT}}$ value of $0.3 \pm$
328 0.1% , Zhu et al., 2016, 2017) was measured before and after each sample to calibrate the mass bias
329 for S isotopes. In situ S isotope measurements were performed at medium mass resolution mode (Zhu
330 et al., 2016, 2017).

331 **Pyrite Iron Isotopes**

332 Based on systematic observation of pyrite morphology, handpicking of large euhedral pyrite
333 grains was carried out and the pyrite grains were cleaned ultrasonically in purified Milli-Q H₂O.
334 About 10 mg handpicked pyrite grains were weighed in a beaker and digested using an acid mixture
335 of ultra-pure concentrated HCl and HNO₃ at 120°C. After evaporation of the HCl and HNO₃, the
336 precipitate was dissolved and evaporated in 0.5 mL concentrated HCl three times. Then the remaining
337 precipitate was diluted in 1.0 mL 6 N HCl. The solution for Fe extraction was purified using AGMP-
338 1 resin, with polyethylene material as the exchange column ($\Phi 6.8 \text{ mm} \times 43 \text{ mm}$). The specific steps
339 of AGMP-1 resin to separate iron in solution are described in Tang (2006a and 2006b). Measurement
340 of Fe isotopes was performed on a Nu-MC-ICP-MS at the MLR Key Laboratory of Deep-Earth
341 Dynamics, Institute of Geology, Chinese Academy of Geological Sciences. Specific method details
342 are provided in Zhu (2002), Zhao (2012), and Fan (2014). Fe isotope values are reported in the
343 standard notation as $\delta^{56}\text{Fe}$ deviation from IRMM-014. In order to monitor the accuracy of the $\delta^{56}\text{Fe}$
344 measurement, both international standard (BHVO-2) and a Chinese standard (CAGSR) were
345 measured together with our samples. The external reproducibility was better than $\pm 0.10\%$ (Zhao et
346 al., 2012; Fan et al., 2014).

347 **Text S4: Background and Interpretation of Geochemical Data**

348 **Fe-speciation**

349 Fe-speciation is a commonly used proxy for reconstructing seawater redox state. Fe_{HR}/Fe_T
350 ratios > 0.38 generally indicate water column anoxia (Raiswell and Canfield, 1998; Canfield et al.,
351 2008; Poulton and Canfield, 2011), whereas ratios in ancient rocks deposited under oxic conditions
352 are generally significantly lower (0.14 ± 0.08 ; Poulton and Raiswell, 2002). However, due to inherent
353 variability in the source rocks deposited in a particular region, wherever possible, an oxic baseline
354 should be derived for the precise rocks being analysed (Raiswell et al., 2008; Poulton, 2021). Values
355 between the oxic baseline and 0.38 are considered equivocal, as rapid deposition (as would likely be
356 the case for the Nantuo Formation diamictites) or post-depositional conversion of unsulfidized Fe_{HR}
357 to poorly reactive Fe minerals may lessen depositional Fe_{HR}/Fe_T ratios (Raiswell and Canfield, 1998;
358 Poulton and Raiswell, 2002). In the case of equivocal Fe_{HR}/Fe_T ratios, additional evidence (e.g.,
359 $\delta^{56}Fe_{py}$ values) may allow oxic and anoxic deposition to be distinguished. Where samples are
360 considered to have been deposited under anoxic conditions, Fe_{py}/Fe_{HR} ratios can be used to provide
361 further insight into seawater redox state, whereby Fe_{py}/Fe_{HR} ratios $> 0.6-0.8$ indicate euxinic
362 conditions (Raiswell and Canfield, 1998; Poulton and Canfield, 2005; Poulton, 2021) and Fe_{py}/Fe_{HR}
363 ratios < 0.6 indicate ferruginous conditions (anoxic, Fe(II)-containing; Poulton et al., 2004; Poulton,
364 2021).

365 **Pyrite Sulphur Isotopes**

366 The S isotope composition ($\delta^{34}S$) of sedimentary pyrite is mainly controlled by the S isotope
367 composition of seawater sulfate and isotopic fractionation between sulfate and sulfide, both of which
368 are essential for understanding the global sulfur cycle and pyrite S isotope systematics. Generally,

369 SO_4^{2-} concentrations in sediments or water column have the greatest impact on sulfur isotope
370 fractionations observed in sedimentary pyrite. When sulfate is present in abundance, microbial sulfate
371 reduction (MSR) can lead to sulfur isotope fractionations of up to 40‰ (Fig. S4). When SO_4^{2-}
372 concentrations are lower, the isotopic fractionation between SO_4^{2-} and H_2S may decrease. For
373 example, when the SO_4^{2-} concentration is lower than 200 μM , MSR has been shown to limit the extent
374 of sulfur isotope fractionation (Habicht et al., 2002).

375 Seawater sulfate, a key factor controlling S isotope fractionation, is mainly derived from the
376 oxidative weathering of sulfide on land, and seawater redox state exerts an influence on the burial
377 flux of sulfur. Thus, the seawater sulfate reservoir (SSR) is closely related to the redox state of the
378 atmosphere and ocean. In addition, $\delta^{34}\text{S}_{\text{py}}$ can provide information about the SSR and isotopic
379 composition of the seawater sulfate. Therefore, $\delta^{34}\text{S}_{\text{py}}$ is an effective general indicator of the size of
380 the SSR (e.g., Canfield, 1998). Although ^{32}S is preferentially -utilized by MSR, sulfur isotope
381 fractionation between sulfate and pyrite can become muted in the presence of limited sulfate supply
382 - leading to the formation of pyrite enriched in ^{34}S . Thus, a high $\delta^{34}\text{S}_{\text{py}}$ value may be linked to a
383 decrease in the SSR, which may be related to the expansion of anoxic waters and increased pyrite
384 burial (Scott et al., 2014).

385 **Pyrite Iron Isotopes**

386 The Fe isotope composition of sedimentary pyrite is controlled by the Fe isotope composition
387 of seawater and subsequent Fe isotopic fractionations during mineral formation, both of which form
388 the basis for explaining the $\delta^{56}\text{Fe}_{\text{py}}$ variability observed in our samples. Seawater Fe is mainly sourced
389 from continental weathering, riverine input, and submarine hydrothermal activity (Anbar and Rouxel,
390 2007), whereby (1) $\delta^{56}\text{Fe}$ values of igneous rocks are relatively uniform, concentrating around 0.1‰

391 (Zhu et al., 2002; Beard et al., 2003); (2) $\delta^{56}\text{Fe}$ values of continental weathering are slightly lower
392 than that of igneous rocks ($\sim -0.1\text{‰}$; Anbar and Rouxel, 2007); (3) $\delta^{56}\text{Fe}$ values of the modern
393 submarine hydrothermal fluid varies from -0.8‰ to 0‰ . (Yamaguchi et al., 2005); (4) Suspended and
394 dissolved iron from rivers accounts for more than 50% of the Fe source to seawater, and $\delta^{56}\text{Fe}$ values
395 range from -1.0‰ to 0‰ (Beard et al., 2003; Ingri et al., 2006); (5) $\delta^{56}\text{Fe}$ values of dissolved Fe
396 released from marginal sea and continental shelf sediments are close to that of igneous rocks
397 (Severmann et al., 2006). In summary, the iron isotopic composition of different sources generally
398 shows a certain degree of light isotope enrichment, explaining low $\delta^{56}\text{Fe}$ values in seawater through
399 the geological history. Sedimentary carbonate rocks are generally believed to record the $\delta^{56}\text{Fe}$
400 composition of seawater (von Blanckenburg et al., 2008). Yan et al. (2011) and Fan et al. (2014; 2018)
401 reported that the $\delta^{56}\text{Fe}$ values of carbonate rocks in the Ediacaran Doushantuo Formation, South
402 China, vary from -0.50‰ to 0‰ . These $\delta^{56}\text{Fe}$ values suggest that seawater in South China during the
403 late Neoproterozoic era was enriched in the lighter iron isotopes. In our work, a $\delta^{56}\text{Fe}$ seawater value
404 of -0.50 to 0‰ has been assumed as a basis for interpreting pyrite iron isotope systematics.

405 The dynamic evolution of $\delta^{56}\text{Fe}_{\text{py}}$ in individual geologic terranes is dominantly interpreted to
406 reflect extensive/partial oxidation of seawater and subsequent iron reduction in sediments (Zhang et
407 al., 2015; Sawaki et al., 2017). Under oxic conditions, nearly all ferrous iron is completely oxidized
408 to ferric (oxyhydr)oxide minerals, minimizing the iron isotopic fractionation (Fig. S4a). The ferric
409 (oxyhydr)oxide is subsequently reduced in anoxic sediments, and may be converted into diagenetic
410 pyrite. The pyrite formed during early diagenesis has $\delta^{56}\text{Fe}$ values similar to, or lower than, seawater
411 (-0.8 to 0‰ ; Severmann et al., 2008), depending on the extent of reduction of the precursor iron
412 (oxyhydr)oxide minerals. Under ferruginous conditions, partial oxidation of ferrous iron may

413 commonly occur (Planavsky et al., 2012), resulting to significant iron isotopic fractionation of ~1 to
414 3‰, and formation of ferric (oxyhydr)oxides with high $\delta^{56}\text{Fe}$ values (Fig. S4b). Pyrite formed through
415 the subsequently reduction of ferric minerals during early diagenesis may display large variability in
416 $\delta^{56}\text{Fe}$ values, ranging from positive to negative, dependent on the $\delta^{56}\text{Fe}$ of the precursor iron
417 (oxyhydr)oxide minerals and the extent of their reduction (Rouxel et al., 2005; Planavsky et al., 2012).
418 Under euxinic (anoxic and sulfidic) conditions, ferrous iron undergoes extensive removal into pyrite,
419 likely invoking an intermediate phase of FeS_m (Fig. S4c). Butler et al. (2005) suggest a kinetic isotopic
420 fractionation (KIE) of $0.85 \pm 0.30\%$ ($\delta^{56}\text{Fe}$ value) during FeS_m precipitation. Heard et al. (2020) also
421 proposed that pyrite precipitation involves KIE, resulting in Fe^{2+} in FeS_2 being enriched in the lighter
422 isotopes relative to $\text{Fe}^{2+}_{(\text{aq})}$. However, as the $\text{FeS}_m\text{-Fe}^{2+}_{(\text{aq})}$ system gradually tends towards
423 equilibrium, the kinetic fractionation value ($\delta^{56}\text{Fe}$ value) between $\text{Fe}^{2+}_{\text{aq}}$ and FeS_m gradually
424 decreases, to $< 0.3\%$, or with no obvious fractionation (Butler et al., 2005; Guilbaud et al., 2010,
425 2011a, b). Thus, in this pathway of pyrite formation without an Fe (oxyhydr)oxide precursor, no
426 significant iron isotopic fractionation occurs, and pyrite formed under euxinic conditions tend to have
427 negative to near-zero $\delta^{56}\text{Fe}$ values (Severmann et al., 2008).

428 Redox state is the most important factor to control the fractionation of iron isotopes in the
429 surface Earth, and pyrite iron isotopes can effectively trace ancient seawater redox conditions. Prior
430 to interpreting $\delta^{56}\text{Fe}_{\text{py}}$ values, a possible detrital influence should be evaluated. Our detailed
431 petrographic investigation did not find any robust evidence for substantial detrital pyrite in the Nantuo
432 Formation at the ZK01 core (see sample description in the Materials and Methods above).
433 Furthermore, the broad co-variation we observe among pyrite Fe isotopes, pyrite S isotopes and Fe-
434 speciation is difficult to be explain unless the pyrite is syngenetic/diagenetic (Fig. 3). In particular,

435 the S isotope were from in-situ analysis of euhedral pyrite, and document progressive changes in
436 isotopic composition that are linked to independent evaluation of water column redox conditions.
437 This suggest that the variable Fe isotopic signatures of the Marinoan pyrite are unlikely to be related
438 to detrital input, and instead reflect a primary signal from syngenetic/diagenetic pyrite.

439 **Text S5: Alternative Hypotheses for Seawater Redox Variability**

440 **Sea-level Elevation**

441 Sea-level elevation, by controlling fluctuations in the depth and position of the chemocline, can
442 lead to variability in the redox state of the local seawater column, whereby sea-level falling and rising
443 may bring the seafloor at the study site into and out of the more oxygenated surface layer of the ocean.
444 Based on the abovementioned glaciation dynamics, ice advance and retreat are associated with sea-
445 level falling and rising. At the study section, the lithofacies and sedimentary characteristics show two
446 distinct ice advance-retreat cycles. For the first cycle, sea-level first falls and then rises during
447 deposition of Units I and Unit II, respectively, bringing the study site into and out of the more
448 oxygenated surface layer. However, all the geochemical data, including Fe-S isotopes and Fe-
449 speciation, indicate the opposite scenario, with deoxygenation and oxygenation occurring in upper
450 part of Unit I and Unit II, respectively (Fig. 3). Similarly, the ice advance recorded in the Unit III
451 corresponds to seawater deoxygenation (Fig. 3). These observations suggest that the redox variability
452 observed during the Marinoan glaciation was not caused by sea-level fluctuations.

453 **Oxygen Input via Open Water**

454 Another possible control on the dynamic redox history concerns the periodic development of
455 open water, leading to enhanced productivity and O₂ production, as well as exchange of O₂ between
456 the atmosphere and ocean. There is increasing evidence for open water conditions during the

457 Cryogenian glaciations. Ye et al. (2015) suggested that local open water conditions allowed the
458 survival of benthic macroscopic phototrophs during the Marinoan glaciation. Elemental
459 characteristics, Fe-speciation, and N-isotope data from Marinoan deposits also indicated expansive
460 regions of open water throughout one of the harshest glaciations in Earth history (Johnson et al.,
461 2017). In addition, red beds, carbonates and shales deposited in open water or glacial lakes have been
462 identified in the glacial deposits (Lang et al., 2018a; Bai et al., 2020; Yan et al., 2020; Shen et al.,
463 2021).

464 On the one hand, open water would enhance the supply of light to fuel photosynthesis, and
465 hence O₂ production via organic matter production and burial. It has been suggested that no obvious
466 mass extinction event is observed at this time from fossil records, biomarker evidence and molecular
467 clock data (Erwin, 2015; Ye et al., 2015), although the low-latitude glaciation has been proposed to
468 present a formidable barrier to the survival of oceanic species (Hoffman et al., 1998). Notably, active
469 primary productivity occurred in the glacial ocean due to the open water (Johnson et al., 2017; Ye et
470 al., 2015). Thus, we can assume that there was a certain amount of biogenically-produced O₂ in the
471 glacial ocean. However, TOC concentrations recorded in our Nantuo Formation samples are low and
472 relatively stable across the Nantuo Formation, giving no indication, at least at the local scale, of
473 productivity-induced changes in O₂ production (Fig. 3).

474 On the other hand, open water allows air sea-gas exchange and oxygen diffusion into the
475 subglacial ocean (Johnson et al., 2017), which could potentially lead to variability in seawater redox
476 conditions. From geochemical calculations and numerical modelling, gas diffusion efficiency has a
477 positive correlation relation with the ice-free surface size of the glacial ocean, but a limited area of
478 open water (10³ km²) can lead to 90% modern efficiency, allowing an efficient gas diffusion into the

479 ocean (Le Hir, 2008a). Thus, equilibration of the atmosphere and ocean due to local open water was
480 likely quite rapid (Le Hir, 2008a), and the chemical properties of seawater would thus change
481 relatively rapidly (Le Hir, 2008b). Furthermore, given that open water is unsustainable because sea
482 ice would become globally extensive within a few thousand years (Hoffman et al., 2017), rapid
483 shutdown of the atmospheric O₂ influx would occur and seawater deoxygenation directly following
484 rapid oxidation would be observed. This could be a prevalent cause of the shorter-term redox
485 variability observed in parts of the Nantuo succession, but appears an unlikely explanation for the
486 longer-term trends that are more closely linked to the broader cycles of glacial advance and retreat
487 (Fig. 3).

488 **Meltwater-derived Oxygen**

489 As mentioned above, meltwaters can be a prominent source of oxygen to the subglacial ocean
490 during ‘Snowball Earth’ events (Lechte et al., 2019). The geochemical evidence we present
491 necessitates an explanation comprising well-oxygenated ice-retreat intervals and anoxic ice-advance
492 intervals across two cycles during the Marinoan glaciation. We suggest that the most parsimonious
493 explanation for these data comprises variable input of oxygen and sulfate from subglacial meltwaters.

494 In the beginning of the first ice advance during the glaciation, the ice sheet formed, and hence
495 atmosphere O₂ influx was suppressed. As the ice became thicker, the influx of meltwater and its
496 resultant O₂ was limited. The transient oxic conditions during this period (lower part of Unit I) could
497 be interpreted as the initial persistence of a well-oxygenated interglacial ocean (Li et al., 2012; Zhang
498 et al., 2015; Peng et al., 2019). With the ongoing first ice-sheet advance, the meltwater and resultant
499 O₂ influx gradually decreased, leading to rapid consumption of seawater sulfate and the oxygen
500 inventory. As a result, deoxygenation occurred and the previous oxic conditions transited to

501 anoxic/ferruginous conditions, albeit with fluctuations in redox state through upper part of Unit I (Fig.
502 3).

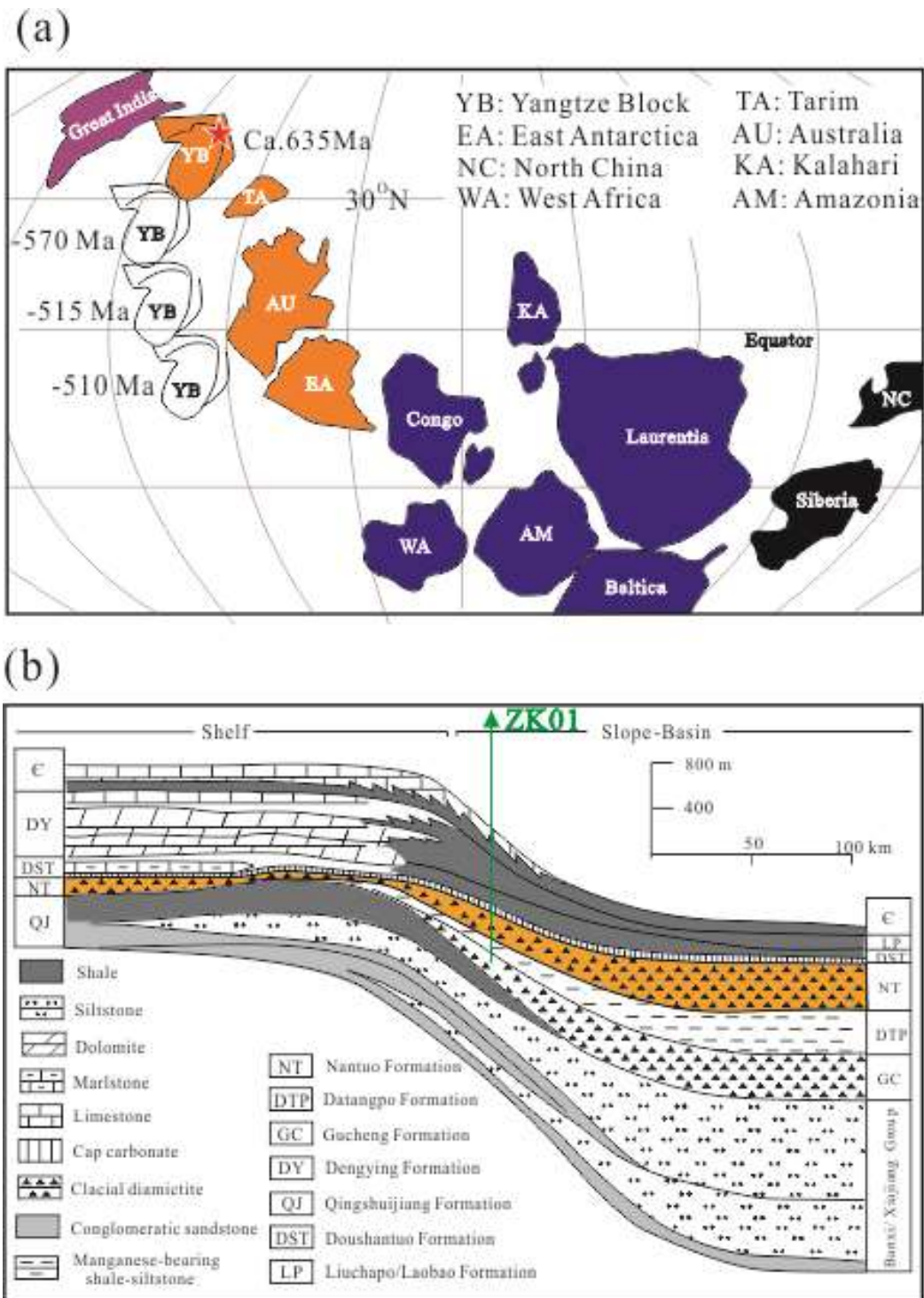
503 When the first ice-sheet retreat occurred, anoxic/ferruginous conditions initially persisted
504 through Unit II (Fig. 3). This increase in oxygenation occurred as the ice experienced its maximum
505 retreat, which was accompanied by an increasingly warm climate, leading to an abundant influx of
506 meltwater and subglacial water-filled rivers/streams containing O₂ (Anderson, 2007; Hoffman et al.,
507 2017).

508 The increase in oxygenation during the ice-sheet retreat period continued during the onset of
509 the second ice sheet advance, but it is terminated by the ongoing of the ice sheet advance. The oxic
510 conditions, interpreted by the finality of the previous seawater oxygenation, evolved into
511 anoxic/ferruginous conditions as the oxygenation level gradually decreased (Fig. 3). With the ongoing
512 of the second ice sheet advance, the climate turned colder and the ice sheet achieved its maximum
513 extent, thus decreasing the oxygen influx from meltwaters. In parallel, oxygen and sulfate would have
514 been consumed from the water column by microbial and abiotic processes, leading to the development
515 of anoxic/ferruginous conditions (Unit III).

516 The second ice retreat then occurred, with a substantial influx of sulfate leading to the
517 development of euxinic conditions recorded in Unit IV (Fig. 3). During this interval, enhanced
518 meltwater could have delivered abundant O₂ into the ocean. Nevertheless, a significant increase in
519 continental weathering, as proposed by the Mg isotopes (Huang et al., 2016), could have consumed
520 oxygen through oxidative weathering, and also delivered nutrients, ultimately resulting in the
521 development of water column euxinia (Lang et al., 2018b).

522 **Spatial Significance**

523 Our $\delta^{56}\text{Fe}_{\text{py}}$ and $\delta^{34}\text{S}_{\text{py}}$ data, as well as the Fe-speciation, record secular variability in seawater
524 redox state during the Marinoan glaciation (Fig. 3). The secular variability in seawater redox state,
525 although may be explained by a combination of meltwater-derived O_2 enhanced, productivity and O_2
526 production, as well as exchange of O_2 between the atmosphere and ocean, is evident in concert with
527 the waxing and waning of the ice sheet (Fig. 4). The above-mentioned glaciation dynamics show the
528 waxing and waning of the ice sheet, as well as the dynamic meltwater-derived O_2 influx, are tightly
529 related to the temperature fluctuations and sea level evolution. Thus, the seawater redox variations
530 deduced from those apparent regional proxies are actually controlled by global events, and as such
531 they are of widespread significance.



532

533 **Figure S1**

534 **Global reconstruction of the location of the Yangtze block and stratigraphic division of the Neoproterozoic**
 535 **transect in the Yangtze block. (a)** Global reconstruction of the location of the Yangtze block and
 536 drift trajectory from ca. 635 to ca. 510 Ma (simplified from Zhang et al., 2015). **(b)** Stratigraphic division of the
 537 Neoproterozoic transect from north to south in the Yangtze block (modified from Jiang et al., 2011). Location of
 538 drill core ZK01 can be seen in Fig. 1a.

539

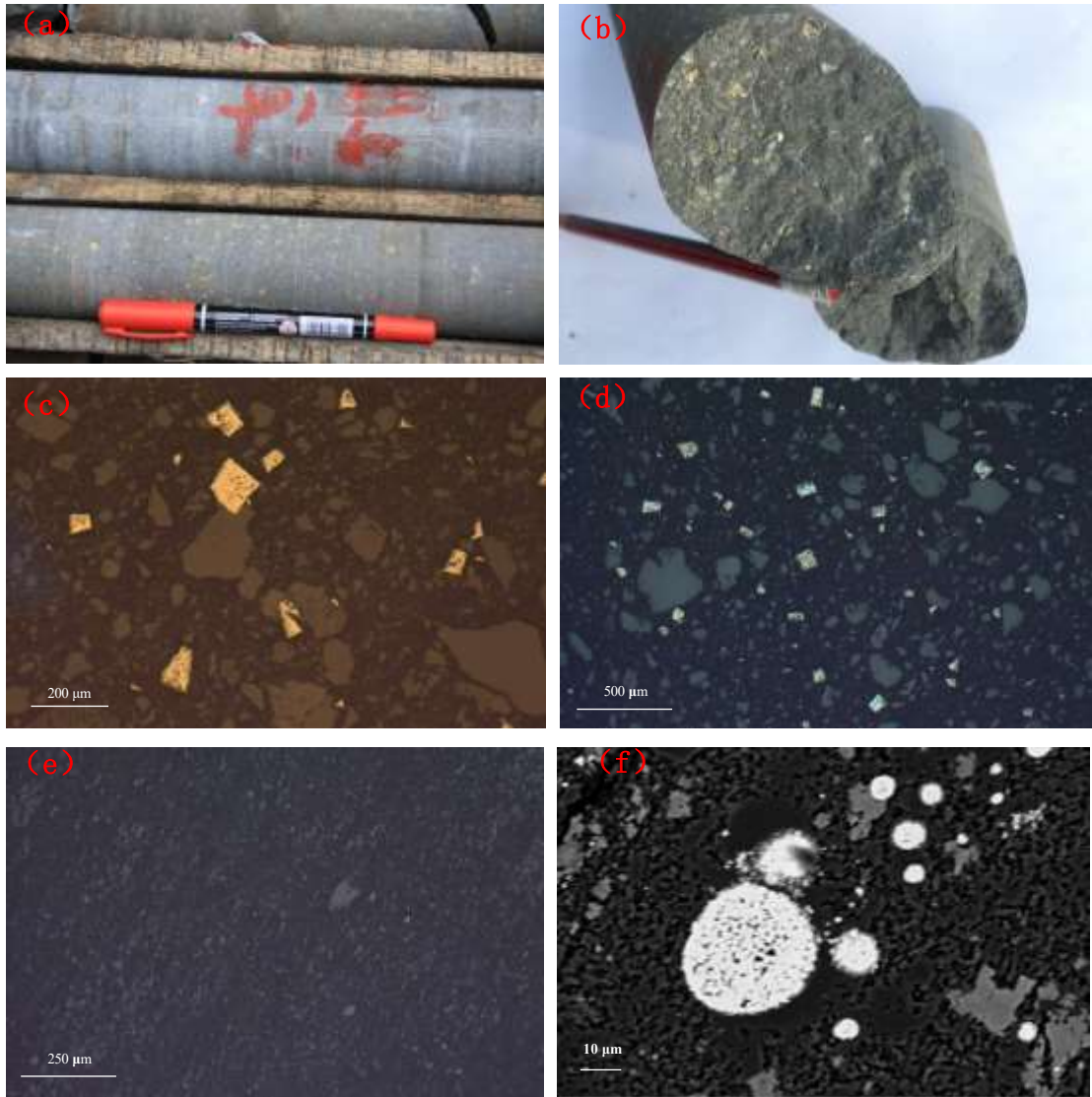


Figure S2

Morphology of pyrite for Nantuo Formation in South China. (a) and (b) show coarse-grained pyrite in hand specimen; (c) and (d) show euhedral pyrite under reflected light. (e) show disseminated pyrite under reflected light; (f) shows pyrite framboids under scanning electron microscope.



Figure S3

Photographs showing lithofacies of the Nantuo Formation from the ZK01 core section. (a) Nantuo Formation conformable over the interglacial Datangpo Formation. **(b)** Manganese ore in the Datangpo Formation. **(c)** Diamictite lithofacies in the first lithological cycle. **(d)** Carbonate rock intervals between the two lithological cycles. **(e)** and **(f)**, Diamictite lithofacies with small and large gravel size/content in the second lithological cycle. **(g)** Nantuo Formation conformably underlies the postglacial Doushantuo Formation. **(h)** Cap carbonate in the Doushantuo Formation.

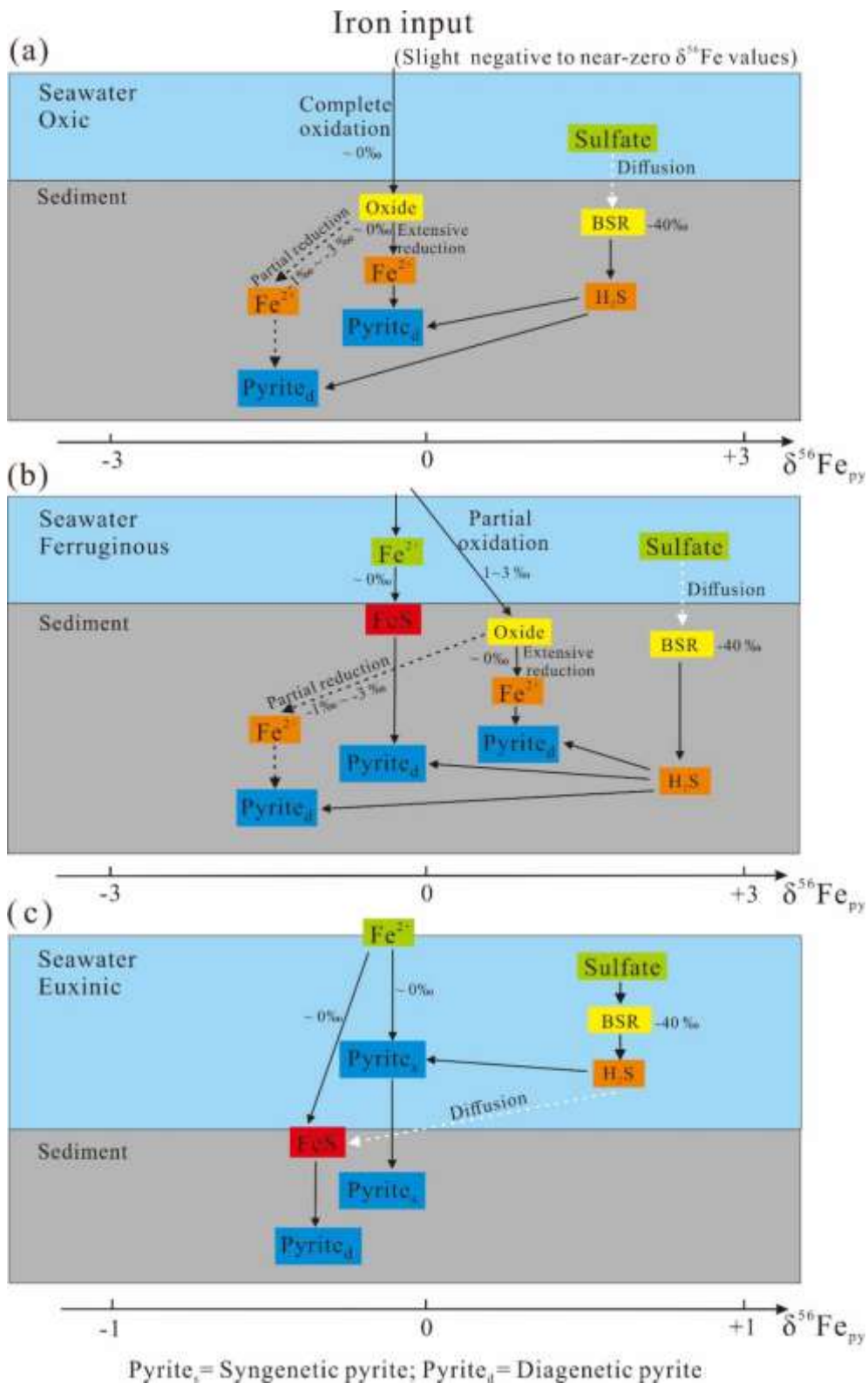


Figure S4

Model showing pyrite formation in the water column and sediments under (a) oxic, (b) ferruginous, and (c) euxinic conditions.

1 **References Cited**

- 2 Alcott, L. J., Krause, A. J., Hammarlund, E. U., 2020. Development of iron speciation reference
3 materials for paleoredox analysis: *Geostandards and Geoanalytical Research* v. 44, p. 581–
4 591.
- 5 Allen, P.A., Etienne, J.L., 2008, Sedimentary challenge to Snowball Earth: *Nat. Geosci.* v. 1, p. 817–
6 825.
- 7 Allen, P.A., Leather, J., and Brasier, M.D., 2004, The Neoproterozoic Fiq glaciation and its
8 aftermath, Huqf supergroup of Oman: *Basin Res.*, v. 16, p. 507 – 534.
- 9 Anbar, A.D., Rouxel, O., 2007, Metal stable isotopes in paleoceanography: *Annu. Rev. Earth Planet.*
10 *Sci.*, v. 35, p. 717–746.
- 11 Anderson, S.P., 2007. Biogeochemistry of Glacial Landscape Systems: *Annu. Rev. Earth Planet. Sci.*
12 v.35, p. 375–99.
- 13 Anderson, S.P., Drever, J.I., Frost, C.D., Holden, P., 2000, Chemical weathering in the foreland of
14 a retreating glacier: *Geochim. Cosmochim. Acta.* v. 7, p. 1173–89
- 15 Anderson, S.P., Longacre, S.A., Kraal, E.R., 2003, Patterns of water chemistry and discharge in the
16 glacier-fed Kennicott River, Alaska: evidence for subglacial water storage cycles: *Chem.*
17 *Geol.*, v. 3–4, p. 297–312
- 18 Armstrong, R.L., 1971, Glacial erosion and the variable isotopic composition of strontium in sea
19 water: *Nature*, v. 230, p. 132–33
- 20 Arnaud, E., Eyles, C.H., 2006, Neoproterozoic environmental change recorded in the Port Askaig
21 Formation, Scotland: Climatic vs tectonic controls: *Sedimentary Geology*, v. 183, p. 99–124.
- 22 Bai, H.Q., Liu, Y.Q., Peng, N. Kuang, H.W., and Wang, Y.C., 2020, Marinoan-aged red beds at
23 Shennongjia, South China: Evidence against global-scale glaciation during the Cryogenian:
24 *Palaeogeography, Palaeoclimatology, Palaeoecology*, v. 559 109967.
25 doi:10.1016/j.palaeo.2020.109967.
- 26 Bao, X., Zhang, S., Jiang, G., Wu, H., Li, H., and Wang, X., 2018, Cyclostratigraphic constraints on
27 the duration of the Datangpo Formation and the onset age of the Nantuo (Marinoan) glaciation
28 in South China: *Earth Planet. Sci. Lett.*, v. 483, p. 52–63.
- 29 Beard, B.L., Johnson, C.M., Von Damm, K.L., Poulson, R.L., 2003, Iron isotope constraints on Fe

30 cycling and mass balance in oxygenated Earth oceans: *Geology*, v. 7, p. 629.

31 Boulton, G. S., Deynoux, M., 1981, Sedimentation in glacial environments and the identification of
32 tills and tillites in ancient sedimentary sequences: *Precambrian Research*, v. 15, p. 397–422.

33 Boyle, R.A., Lenton, T.M., Williams, H.T.P., 2007, Neoproterozoic ‘snowball Earth’ glaciations and
34 the evolution of altruism: *Geobiology*, v. 5, p. 337–349

35 Brodzikowski, K., Van Loon, A., 1987, A systematic classification of glacial and periglacial
36 environments, facies and deposits: *Earth–Science Reviews*, p. 297–381.

37 Brown, G., Tranter, M., Sharp M., Davies T., and Tsiouris S., 1994, Dissolved oxygen variations in
38 Alpine glacial meltwaters: *Earth Surface Processes and Landforms*, v. 19, p. 247–253.

39 Butler, I.B., Archer, C., Vance, D., Oldroyd, A., Rickard, D., 2005, Fe isotope fractionation on FeS
40 formation in ambient aqueous solution: *Earth Planet. Sci. Lett.*, v. 236, p. 430–442.

41 Canfield, D.E., 1998, A new model for Proterozoic ocean chemistry: *Nature*, v. 396, p. 450–452

42 Canfield, D.E., Poulton, S.W., Knoll, A.H., et al., 2008, Ferruginous Conditions Dominated Later
43 Neoproterozoic Deep–Water Chemistry: *Science*, v. 321, p. 949–952.

44 Canfield D.E., Raiswell R., Westrich J.T., Reaves C.M. and Berner R. A., 1986, The use of
45 chromium reduction in the analysis of reduced inorganic sulfur in sediments and shales: *Chem.*
46 *Geol.* V. 54, p. 149–155.

47 Condon, D.J., Zhu, M.Y., Bowring, S., Wang, W., Yang A.H., and Jin, Y.G., 2005, U–Pb ages from
48 the Neoproterozoic Doushantuo Formation, China: *Science* v. 308, p. 95–98.

49 Collins, D.N., MacDonald, O.G., 2004, Year–to–year variability of solute flux in meltwaters
50 draining from a highly–glacierized basin: *Nordic Hydrol.*, v. 4–5, p. 359–67

51 Chumakov, N.M., 2009, Neoproterozoic glacial events in Eurasia. In: Gaucher, C., Sial, A.N.,
52 Halverson, G.P., Frimmel, H.E. (Eds.): *Neoproterozoic–Cambrian Tectonics, Global Change*
53 *and Evolution: a focus on southwestern Gondwana. Developments in Precambrian Geology*
54 16, Elsevier, pp. 389–403.

55 Erwin, D. H., 2015, Early metazoan life: Divergence, environment and ecology: *Philos. Trans. R.*
56 *Soc. Lond. B Biol. Sci.*, v. 370, p. 36.

57 Fan, H.F., Wen, H.J., Zhu, X.K., Feng, L.J., and Chang, H.J., 2018, Oceanic redox condition during
58 the late Ediacaran (551–541 Ma), South China: *Geochimica et Cosmochimica Acta*, v. 238,

59 p. 343–356.

60 Fan, H.F., Zhu, X.K., Wen, H.J., Yan, B., Li, J., and Feng, L.J., 2014, Oxygenation of Ediacaran
61 Ocean recorded by iron isotopes: *Geochim. Cosmochim. Acta*, v. 140, p. 80–94.

62 Gu S., Fu Y. and Long J., 2019, Predominantly Ferruginous Conditions in South China during the
63 Marinoan Glaciation: Insight from REE Geochemistry of the Syn-glacial Dolostone from the
64 Nantuo Formation in Guizhou Province, China: *Minerals*, v. 9.

65 Guilbaud, R., Butler, I.B., Ellam, R.M., Rickard, D., Oldroyd, A., 2011a. Experimental
66 determination of the equilibrium Fe isotope fractionation between $\text{Fe}^{2+}_{\text{aq}}$ and FeS_m
67 (mackinawite) at 25 and 2°C: *Geochim. Cosmochim. Acta*, v. 75, p. 2721–2734.

68 Guilbaud, R., Butler, I.B., Ellam, R.M. 2011b. Abiotic pyrite formation produces a large Fe isotope
69 fractionation: *Science*, v. 332, p. 1548–1551.

70 Guilbaud, R., Butler, I.B., Ellam, R.M., Rickard, D., 2010, Fe isotope exchange between $\text{Fe(II)}_{\text{aq}}$
71 and nanoparticulate mackinawite (FeS_m) during nanoparticle growth: *Earth Planet. Sci. Lett.*,
72 v. 300, p. 174–183.

73 Habicht, K.S., Gade, M., Thamdrup, B., Berg, P., Canfield, D.E., 2002, Calibration of Sulfate Levels
74 in the Archean Ocean: *Science*, v. 298, p. 2372–2374.

75 Hambrey, M.J., Glasser, N. F., 2012, Discriminating glacier thermal and dynamic regimes in the
76 sedimentary record: *Sedimentary Geology*, p. 1–33.

77 Hallet, B., Hunter, L., Bogen, J., 1996, Rates of erosion and sediment evacuation by glaciers: a
78 review of field data and their implications: *Global Planet. Change*, v. 12, p. 213–35

79 Halverson, G.P., Maloof, A.C., Hoffman, P.F., 2004, The Marinoan glaciation (Neoproterozoic) in
80 Svalbard: *Basin Res.*, v. 16, p. 297–324.

81 He, J.Y., Xu, B., Meng, X.Y., Kou, X.W., Liu, B., Wang, Y., Mi, H., 2007, Neoproterozoic sequence
82 stratigraphy and correlation in Quluqtagh area, Xinjiang: *Acta Petrologica Sinica*, v. 7, p.
83 1645–1654.

84 Heard, A.W., Dauphas, N., Guilbaud, R., Rouxel, O.J., Butler I.B., Nie, N.X., Bekker, A., 2020,
85 Triple iron isotope constraints on the role of ocean iron sinks in early atmospheric
86 oxygenation, *Science*, v. 370, p. 446–449.

87 Hoffman, P.F., Schrag, D.P., 2002, The snowball Earth hypothesis: testing the limits of global change:

88 Terra Nova, v. 14, p. 129–155.

89 Hoffman, P.F., Kaufman, A.J., Halverson, G.P., Schrag, D.P.A., 1998, Neoproterozoic Snowball
90 Earth: Science, v. 281, p. 1342–1345.

91 Hoffman, P.F., Abbot, D.S., Ashkenazy, Y., Benn, D.I., Brocks, J.J., Cohen, P.A., Cox, G. M.,
92 Creveling, J.R., Donnadieu, Y., Erwin, D.H., Fairchild, I.J., Ferreira, D., Goodman, J.C.,
93 Halverson, G.P., Jansen, M.F., Le Hir, G., Love, G.D., Macdonald, F. A., Maloof, A.C., Partin,
94 C.A., Ramstein, G., Rose, B.E.J., Rose, C.V., Sadler, P.M., Tziperman, E., Voigt, A., Warren,
95 S.G., 2017a, Snowball Earth climate dynamics and Cryogenian geology–geobiology: Sci.
96 Adv. v. 3, p. 1–43.

97 Hoffman, P.F., Lamothe, K.G., LoBianco, S.J.C., Hodgskiss, M.S.W., Bellefroid, E.J., Johnson,
98 B.W., Hodgin, E.B., and Halverson, G.P., 2017b. Sedimentary depocenters on Snowball Earth:
99 Case studies from the Sturtian Chuos Formation in northern Namibia: Geosphere, v. 13, p.
100 811–837.

101 Hu, C.L., Zhu, M.Y., 2020, Lithofacies and glacio–tectonic deformation structures of the
102 Tiesi’ao/Dongshanfeng Formation on the Yangtze Block, South China: Implications for
103 Sturtian Glaciation dynamics: Palaeogeography, Palaeoclimatology, Palaeoecology,
104 <https://doi.org/10.1016/j.palaeo.2019.109481>.

105 Huang, K.J., 2016, Episode of intense chemical weathering during the termination of the 635–Ma
106 Marinoan glaciation. Proc. Natl Acad. Sci. v. 113, p. 14904–14909.

107 Hyde, W.T., Crowley, T.J., Baum, S.K., Peltier, W.R., 2000, Neoproterozoic ‘snowball
108 Earth’ simulations with a coupled climate/ice–sheet model: Nature, v. 405, p. 425–429.

109 Ingri, J., Malinovsky, D., Rodushkin, I., et al. 2006, Iron isotope fractionation in river colloidal
110 matter: Earth and Planetary Science Letters, v. 245, p. 792–798.

111 Irvine - Fynn, T. D., Hodson, A. J., Moorman, B. J., Vatne, G., Hubbard, A. L., 2011, Polythermal
112 glacier hydrology: A review. Reviews of Geophysics, v. 4, p. RG4002.

113 Jenkins, A., 1999, The impact of melting ice on ocean waters: Journal of Physical Oceanography, v.
114 29, p. 2370–2381.

115 Jiang, G.Q., Shi, X.Y., Zhang, S.H., Wang, Y., and Xiao, S.H., 2011, Stratigraphy and
116 paleogeography of the Ediacaran Doushantuo Formation (ca. 635–551 Ma) in South China:
117 Gondwana Research, v. 19, p. 831–849.

118 Johnson, B.W., Poulton, S.W., and Goldblatt, C., 2017, Marine oxygen production and open water
119 supported an active nitrogen cycle during the Marinoan Snowball Earth: *Nature*
120 *Communication*, v. 8, p. 1316–1322.

121 Kirschvink, J.L., 1992, Late Proterozoic low–latitude global glaciation: the snowball Earth. In: *The*
122 *Proterozoic Biosphere: a multidisciplinary study*: Cambridge University Press, New York, pp.
123 51–52.

124 Labaj, M.A., and Pratt, B.R., 2016, Depositional dynamics in a mixed carbonate–siliciclastic system:
125 middle–upper Cambrian Abrigo Formation, Southeastern Arizona, U.S.A: *J. Sediment. Res.*,
126 v. 86, p. 11–37.

127 Lan, Z., Li, X.H., Zhang, Q., and Li, Q.L., 2015, Global synchronous initiation of the 2nd episode
128 of Sturtian glaciation: SIMS zircon U–Pb and O isotope evidence from the Jiangkou Group,
129 South China: *Precamb. Res.*, v. 267, p. 28–38.

130 Lang, X.G., Shen, B., Peng, Y.B., Xiao, S.H., Zhou, C.M., Bao, H.M., Kaufman, A.J., Huang, K.J.,
131 Crockford, P.W., Liu, Y.G., Tang, W.B., and Ma, H.R., 2018b, Transient marine euxinia at the
132 end of the terminal Cryogenian glaciation: *Nature communication*, v. 9, p. 3019.

133 Lang, X.G., Chen, J.T., Cui, H., Man, L. Huang, K.J., Fu, Y., Zhou, C.M., and Shen, B., 2018a,
134 Cyclic cold climate during the Nantuo Glaciation: Evidence from the Cryogenian Nantuo
135 Formation in the Yangtze Block, South China: *Precamb. Res.*, v. 310, p. 243–255.

136 Lechte, M.A., Wallace, M.W., Hood, A.S., Li, W.Q., and Planavsky, N.J., 2019, Subglacial
137 meltwater supported aerobic marine habitats during Snowball Earth: *Proc. Natl. Acad. Sci.*,
138 v. 51, p. 25478–25483.

139 Le Heron, D.P., Busfield, M.E., Prave, A.R., 2014, Neoproterozoic ice sheets and olistoliths:
140 multiple glacial cycles in the Kingston Peak Formation California: *J. Geol. Soc.*, v. 171, p.
141 525–538.

142 Le Hir, G., Ramstein, G., Donnadieu, Y., and Godd eris, Y., 2008a, Scenario for the evolution of
143 atmospheric pCO₂ during a snowball earth: *Geology*, v. 36, p. 47–50.

144 Le Hir, G., Godderis, Y., Donnadieu, Y., Ramstein, G., 2008b, A geochemical modelling study of
145 the evolution of the chemical composition of seawater linked to a “snowball” glaciation:
146 *Biogeosciences*, v. 5, p. 253–267.

147 Lewis, E., Perkin, R., 1986, Ice pumps and their rates. *Journal of Geophysical Research: Oceans*, p.

148 11756–11762.

149 Li, C., Love, G.D., Lyons, T.W., Scott, C.T., Feng, L.J., Huang, J., Chang, H.J., Zhang, Q.R., Chu,
150 X.L., 2012, Evidence for a redox stratified Cryogenian marine basin, Datangpo Formation,
151 South China: *Earth and Planetary Science Letters*, v. 331–332, p. 246–256

152 Liu, Y.G., Yang, J., Bao, H.M., Shen, B., Hu, Y.Y., 2020, Large equatorial seasonal cycle during
153 Marinoan snowball Earth. *Sci. Adv.* 23, eaay2471. <https://doi.org/10.1126/sciadv.aay2471>.

154 Naish, T., et al., 2009, Obliquity–paced Pliocene West Antarctic ice sheet oscillations: *Nature*, v.
155 458, p. 322.

156 Paterson S. B., *The physics of glaciers* (Elsevier, 2016).

157 Peng, X. Zhu, X.K., Shi, F.Q., Yan, B., Zhang, F.F., Zhao, N.N., Peng, P.A., Li, J., Wang, D., and
158 Shields, G.A., 2019, A deep marine organic carbon reservoir in the non–glacial Cryogenian
159 ocean (Nanhua Basin, South China) revealed by organic carbon isotopes: *Precambrian*
160 *Research*, v. 320, p. 212–220.

161 Piotrowski, J. A., 1997, Subglacial hydrology in north–western Germany during the last glaciation:
162 groundwater flow, tunnel valleys and hydrological cycles: *Quaternary Science Reviews*, v.
163 82, p. 169–185.

164 Planavsky, N., Rouxel, O.J., Bekker, A., Hofmann, A., Little, C.T.S., and Lyons, T.W., 2012, Iron
165 isotope composition of some Archean and Proterozoic iron formations: *Geochimica et*
166 *Cosmochimica Acta*, v. 80, p. 158–169.

167 Poulton, S.W., Fralick, P.W., Canfield, D.E., 2004, The transition to a sulphidic ocean~1.84 billion
168 years ago: *Nature*, v. 431, p. 173–177.

169 Poulton, S.W., Canfield, D.E., 2011, Ferruginous Conditions: A Dominant Feature of the Ocean
170 through Earth's History: *Elements*, v. 7, p. 107–112.

171 Poulton, S. W., and Canfield, D. E., 2005, Development of a sequential extraction procedure for
172 iron: implications for iron partitioning in continentally derived particulates: *Chem. Geol.*, p.
173 209–221.

174 Poulton, S. W., and Raiswell, R., 2002, The low-temperature geochemical cycle of iron: From
175 continental fluxes to marine sediment deposition. *American Journal of Science*, v. 302, p.
176 774–805

177 Poulton, S. W., 2021, The Iron Speciation Paleoredox Proxy: *Elements in Geochemical Tracers in*

178 Earth System Science: New York, Cambridge University Press, 1–19 p.

179 Raiswell, R., and Canfeld, D.E., 1998, Sources of iron for pyrite formation in marine sediments:
180 American journal of science, v. 298, p. 219–245.

181 Raiswell, R., Newton, R., Bottrell, S.H., Coburn, P.M., Briggs, D.E.G., Bond, D.P.G., Poulton, S.W.,
182 2008. Turbidite depositional influences on the diagenesis of Beecher's Trilobite Bed and the
183 Hunsruck Slate; sites of soft tissue pyritization. *Am. J. Sci.*, v. 308, p. 105–129.

184 Rooney, A.D., Strauss, J.V., Brandon, A.D., Macdonald, F.A., 2015, A Cryogenian chronology: Two
185 long-lasting synchronous Neoproterozoic glaciations: *Geology*, v. 43, p. 459–462.

186 Rouxel, O.J., Bekker, A., and Edwards, K., 2005, Iron isotope constraints on the Archean and
187 Paleoproterozoic ocean redox state: *Science*, v. 307, p. 1088–1091.

188 Schmitz, M.D., 2012, Appendix 2—Radiometric ages used in GTS3012, in Gradstein, F., Ogg, J.,
189 Schmitz, M.D., and Ogg, G., eds., *The Geologic Time Scale 2012*: Boston, Elsevier, p.1045–
190 1082.

191 Scott, C., Wing, B.A., Bekker, A., Planavsky, N.J., Medvedev, P., Bates, S.M., Yun, M., and Lyons,
192 T.W., 2014, Pyrite multiple-sulfur isotope evidence for rapid expansion and contraction of the
193 early Paleoproterozoic seawater sulfate reservoir: *Earth and Planetary Science Letters*, v. 389,
194 p. 95–104.

195 Severmann, S., Johnson, C. M., Beard, B. L., McManus, J. 2006, The effect of early diagenesis on
196 the Fe isotope compositions of porewaters and authigenic minerals in continental margin
197 sediments: *Geochim. Cosmochim. Acta*, v. 70, p. 2006–2022.

198 Severmann, S., Lyons, T.W., Anbar, A., McManus, J., and Gordon, G., 2008, Modern iron isotope
199 perspective on the benthic iron shuttle and the redox evolution of ancient oceans: *Geology*, v.
200 36, p. 487–490.

201 Sharp, M., Tranter, M., Brown, G.H., Skidmore, M., 1995, Rates of chemical denudation and CO₂
202 drawdown in a glacier-covered alpine catchment: *Geology*, v. 23, p. 61–64

203 Shen, W.B., Zhu, X.K., Yan, B., Qin, H.Y., Gao, Z.F., Li, F.B., 2021, Sequence stratigraphy of the
204 Cryogenian Nantuo Formation in South China: Constraints on Marinoan glaciation dynamics:
205 *Journal of Asian Earth Sciences*, v. 214, p. 104776.

206 Shields, G. A., 2005, Neoproterozoic cap carbonates: A critical appraisal of existing models and the

207 plumeworld hypothesis: *Terra Nova*, v. 17, p. 299–310 2005.

208 Skidmore, M. L., Sharp, M. J., 1999, Drainage system behaviour of a High–Arctic polythermal
209 glacier: *Annals of Glaciology*, p. 209–215.

210 Sawaki, Y., Tahata, M., Komiya, T., Hirata, T., Han, J., and Shu, D.G., 2018. Redox history of the
211 Three Gorges region during the Ediacaran and Early Cambrian as indicated by the Fe isotope:
212 *Geoscience Frontiers*, v. 9, p. 155-172.

213 Talling P.J., Masson D.G., Sumner E.J. and Malgesini G., 2012, Subaqueous sediment density flows:
214 Depositional processes and deposit types: *Sedimentology*, v. 59, p. 1937 – 2003.

215 Tang, S.H., and Zhu, X.K., 2006a, Separation of some element using AG MP–1 anion exchange
216 resin: *Geological journal of China university*, v. 3, p. 398–403.

217 Tang, S.H., Zhu, X.K., Cai, J.J., Li, S.Z., He, X.X., and Wang, J.H., 2006b, Chromatographic
218 separation of Cu, Fe and Zn using AG MP–1 anion exchange resin for isotope determination
219 by MC–ICPMS: *Rock and mineral analysis*, v. 1, p. 5–8.

220 Tostevin, R., Turchyn, A.V., Farquhar, J., et al. 2014, Multiple sulfur isotope constraints on the
221 modern sulfur cycle, *Earth and Planetary Science Letters*, v. 396, p. 14–21

222 Tranter et al., 1997, Variability in the chemical composition of in situ subglacial meltwaters:
223 *Hydrological Processes*, p. 59–77.

224 Tucker, M.E., Paul Wright, V., and Dickson, J.A.D., 1990, *Carbonate Sedimentology*. Blackwell p.
225 28–67.

226 von Blanckenburg, F., Mamberti, M., Schoenberg, R., et al. 2008, The iron isotope composition of
227 microbial carbonate: *Chemical Geology*, v. 249, P. 113–128.

228 Wang, D., Zhu, X.K., Zhao, N.N., Yan, B., Li, X.H., Shi, F.Q., and Zhang, F.F., 2019, Timing of the
229 termination of Sturtian glaciation: SIMS U–Pb zircon dating from South China: *J. Asian Earth*
230 *Sci.*, v. 177, p. 287–294.

231 Wang, J., and Li, Z.X., 2003, History of Neoproterozoic rift basins in South China: implications for
232 Rodinia break–up: *Precambrian Research*, v. 122, p. 141–158.

233 Williams, G.E., Gostin, V.A., McKirdy, D.M., Preiss, W.V., 2008, The Elatina glaciation, Late
234 Cryogenian (Marinoan Epoch), South Australia: Sedimentary facies and palaeoenvironments:
235 *Precambr. Res.* V. 163, P. 307–331.

236 Yamaguchi, K. E., Johnson, C. M., Beard, B. L., and Ohmoto, H., 2005, Biogeochemical cycling of

237 iron in the Archean–Paleoproterozoic Earth: constraints from iron isotope variations in
238 sedimentary rocks from the Kaapvaal and Pilbara Cratons: *Chem. Geol.*, v. 218, p. 135-169.

239 Yan, B., 2011, *Geochemical characteristics of carbonate rocks and black shale in Doushantuo*
240 *Formation of Ediacaran System, South China*. Beijing: Doctoral dissertation of China
241 University of Geosciences (Beijing).

242 Yan, B., Shen, W.B., Zhao, N.N., and Zhu, X.K., 2020, Constraint on the nature of Marinoan
243 glaciation: Cyclic sedimentary records of the Nantuo Formation, South China: *Journal of*
244 *Asian Earth Sciences*, v.189, 104137 (1–13).

245 Ye, Q., Tong, J.N., Xiao, S.H., Zhu, S.X., An, Z.H., Tian, L., and Hu, J., 2015, The survival of
246 benthic macroscopic phototrophs on a Neoproterozoic snowball Earth: *Geology*, v. 43, p.
247 507–510.

248 Zhang, F.F., Zhu, X.K., Yan, B., Kendall, B., Peng, X., Li, J., Algeo, T.J., and Romaniello, S., 2015.
249 Oxygenation of a Cryogenian ocean (Yangtze Basin, South China) revealed by pyrite Fe
250 isotope compositions: *Earth Planet. Sci. Lett.*, v. 429, p. 11–19.

251 Zhang, Q. R., Chu, X. L., and Feng, L.J., 2011, Chapter 32 Neoproterozoic glacial records in the
252 Yangtze Region, China. In: Arnaud, E., Halverson, G.P., Shields–Zhou, G. (Eds.), *The*
253 *Geological Record of Neoproterozoic Glaciations*. vol. 36. Geological Society, London,
254 *Memoirs*, v. 36, p. 357–366.

255 Zhang, S., Jiang, G., and Han, Y., 2008, The age of the Nantuo Formation and Nantuo glaciation in
256 South China: *Terra Nova*, v. 20, p. 289–294.

257 Zhao, J.H., Jin, Z.J., Hu, Q.H., Liu, K.Y., and Wang, R.Y., 2019, Geological controls on the
258 accumulation of shale gas: A case study of the early Cambrian shale in the Upper Yangtze
259 area: *Marine and petroleum geology*, v. 107, p. 423–437.

260 Zhao, X.M., Zhang, H.F., Zhu, X.K., Tang, S.H., and Yan, B., 2012, Iron isotope evidence for
261 multistage melt–peridotite interactions in the lithospheric mantle of eastern China: *Chem.*
262 *Geol.*, v. 292–293, p. 127–139.

263 Zhou, C.M., Tucker, R., Xiao, S.H., Peng, Z.X., Yuan, X.L., and Chen, Z., 2018, New constraints
264 on the ages of Neoproterozoic glaciations in south China: *Geology*, v. 32, p. 437–440.

265 Zhu, X.K., Guo, Y., Williams, R.J.P., O’Nions, R.K., Matthews, A., Belshaw, N.S., Canters, G.W.,
266 Waal de, E.C., Weser, U., and Burgess, B.K., 2002, Mass fractionation processes of transition

267 metal isotopes: *Earth Planet. Sci. Lett.*, v. 200, p. 47–62.

268 Zhu, Z.Y., Jiang, S.Y., Ciobanu, C.L., Yang, T., Cook, N.J., 2017, Sulfur isotope fractionation in
269 pyrite during laser ablation: Implications for laser ablation multiple collector inductively
270 coupled plasma mass spectrometry mapping: *Chemical Geology*, v. 450, p. 223–234

271 Zhu, Z.Y., Cook, N.J., Yang, T., Ciobanu, C.L., Zhao, K.D., and Jiang, S.Y., 2016, Mapping of sulfur
272 isotopes and trace elements in sulfides by LA–(MC)–ICP–MS: Potential Analytical Problems,
273 Improvements and Implications: *Minerals*, v. 110, p. 1–14.

274